ADVANCED MATERIALS
www.advmat.de

Natural Polyphenolic Nanodots for Alzheimer's Disease Treatment

Peng Yang, Qianqian Huang, Jianhua Zhang, Yiwen Li, Huile Gao, and Zhipeng Gu**

The abnormal amyloid-β accumulation is essential and obbligato in Alzheimer's disease pathogenesis and natural polyphenols exhibit great potential as amyloid aggregation inhibitors. However, the poor metabolic stability, low bioavailability, and weak blood–brain barrier crossing ability of natural polyphenol molecules fail to meet clinical needs. Here, a universal protocol to prepare natural polyphenolic nanodots is developed by heating in aqueous solution without unacceptable additives. The nanodots are able to not only inhibit amyloid-β fibrillization and trigger the fibril disaggregation, but mitigate the amyloid-β-plaque-induced cascade impairments including normalizing oxidative microenvironment, altering microglial polarization, and rescuing neuronal death and synaptic loss, which results in significant improvements in recognition and cognition deficits in transgenic mice. More importantly, natural polyphenolic nanodots possess stronger antiamyloidogenic performance compared with small molecule, as well as penetrate the blood–brain barrier. The excellent biocompatibility further guarantees the potential of natural polyphenolic nanodots for clinical applications. It is expected that natural polyphenolic nanodots provide an attractive paradigm to support the development of the therapeutics for Alzheimer's disease.

1. Introduction

Alzheimer's disease (AD), the primary cause of dementia, has quickly become one of the most common fatal diseases lacking an efficiency treatment of this century. It was expected that the number of people living with dementia worldwide would exceed 150 million by 2050,[1] which not only causes huge burdens and pain to patients and medical staffs, but requests significant financial expenditures.[2] The formation of amyloid-beta (Aβ) plaques has been regarded as the central event in AD pathology,[3] triggering the following tau deposition, neuroinflammation, neuron and synaptic loss, and cognitive decline, which is supported by the neuropathological and human genetic evidence.[4] In AD condition, the abnormal Aβ accumulation triggers proinflammatory response and inflammatory factors generation. In turn, inflammatory microenvironment causes more Aβ accumulation and microglia dysfunction, which strictly promotes AD progression.[5] Also, tau protein is hyperphosphorylated and accumulated to form neurofibrillary tangles with toxicity, causing severe neuron and synaptic loss.[6] Aimed at lowering the level of Aβ plaque deposition, several potential therapeutics have been proceeded and the Aβ-targeted monoclonal antibody (aducanumab) has been approved fast by the U.S. Food and Drug Administration (FDA), however, which has been controversial due to its unclear therapeutic effects that the negative trial results were not related with amyloid hypothesis directly and necessarily.[7] A growing body of researches have indicated that the therapeutic strategies targeting Aβ is necessary but insufficient.[8] Thus, a consensus viewpoint is that the development of effective Aβ-targeted agents with more targeting pathological mechanisms is imperative.

Until now, various substances have been employed to intercept Aβ aggregation and alleviate Aβ-induced oxidative stress, metal dysregulation, and neurotoxicity, including peptides, antibodies, antibiotics, multifunctional molecules, and nanoparticles (NPs).[9] However, many ingredients possessed palliative therapeutic effects in vivo although they showed active capacity in testing tube.[10] In the past years, increasing attention has been paid to natural compounds, especially natural polyphenols, which are wealth of sources, high availability, and low toxicity, making these compounds promising candidates for the safe treatment at the initial stage of AD therapy.[11] It has been proved that natural

P. Yang, J. Zhang, Y. Li, Z. Gu
College of Polymer Science and Engineering
State Key Laboratory of Polymer Materials Engineering
Sichuan University
Chengdu 610065, China
E-mail: guzhipeng2019@scu.edu.cn
P. Yang
Department of Health Products Technical Research and Development Center
Yunnanbaiyao Group Co. Ltd.
Kunming 650500, China
Q. Huang, H. Gao
Key Laboratory of Drug-Targeting and Drug Delivery System of the Education Ministry
Sichuan Engineering Laboratory for Plant-Sourced Drug and Sichuan Research Center for Drug Precision Industrial Technology
West China School of Pharmacy
Sichuan University
Chengdu 610064, China
E-mail: gaohuile@scu.edu.cn

The ORCID identification number(s) for the author(s) of this article can be found under https://doi.org/10.1002/adma.202308393

DOI: 10.1002/adma.202308393

polyphenols can not only suppress the misfolding and aggregation of protein, but act downstream of amyloid plaques to prevent cascade toxic including but not limited to inflammation, imbalance of metal ions, and protein homeostasis.[12] Yet, small molecular natural polyphenolic compounds failed to satisfy the clinical study due to their metabolic instability and poor bioavailability, which is an indispensable for brain treatment since the drugs need to cross the blood–brain barrier (BBB) and meet the concentration requirements of treatment.[13] Nanotechnological approaches might be alternative and the elegant structure of natural polyphenols makes them to fabricate robust and multifunctional nanomaterials easily, which can cross BBB well with prolonged circulation time under suitable conditions. Notably, the particle size beyond 5 nm can avoid the renal clearance and prolong the blood circulation time, which improved the probability of the interaction between particle and BBB causing the following transcytosis to brain, but the larger particles (>50 nm) would be removed by the liver and/or spleen finally.[14] However, the established methods for natural polyphenolic nanomaterial synthesis involve complicated preparation processes and introduction of additional agents needs reforming.[15] Hence, the exploration of natural polyphenolic nanomaterials with efficient and universal synthesis methodologies would greatly contribute to the promising possibilities opened by the employment of natural polyphenols for AD treatment.

Herein, a general and modular strategy to synthesize natural polyphenolic nanodots (NDs) is presented by heating in aqueous solution (**Figure 1**a). We carefully investigated the formation of NDs, which was contributed by the physical assembly of monomer and the occurrence in parallel of oxidative polymerization. The obtained NDs can inhibit Aβ fibrillization effectively, as well as disaggregate the preformed Aβ fibrils. More importantly, natural polyphenolic NDs exhibited enhanced antiamyloidogenic performance compared with small molecule due to the multiple binding points of the NDs, as demonstrated by in vitro experiments. Encouragingly, the NDs were applied in amyloid precursor protein/presenilin-1 (APP/PS1) mice model, where the progressive Aβ plaque deposition and cognitive decline of the mice were reversed. This work not only clarified the formation mechanisms of natural polyphenolic NDs accelerated by heat, but offered a bright avenue of natural polyphenols for AD therapy.

2. Results and Discussion

2.1. Preparation and Characterization of Natural Polyphenolic NDs

Natural polyphenolic NDs were easily prepared by heating at 80°C in aqueous solution. After purification, the collected NDs showed uniform morphologies with the diameter in the range of 3–12 nm (Figure 1b and Figure S1a,b (Supporting Information)), which might be caused by the inherent chemical structure of different natural polyphenols. An interesting event is that all samples possessed lamellar structure with an interlayer spacing of ≈0.21 nm, indicating the presence of supramolecular assembly structure in NDs,[15c] and the X-ray diffraction pattern indicated that the NDs were amorphous (Figure S1c, Supporting Information). Note that the reported approach possessed generality and modularity for water-soluble natural polyphenols. Taking gallic acid (GA)-based NDs as a representative sample, the kinetics of heat-triggered oxidative polymerization were investigated by UV absorbance monitoring. As shown in Figure S1d (Supporting Information), the color of GA solution was changed and gradually deepened when heated while the solution color remained stable at room temperature. UV spectra of heated GA solution also shifted to higher absorbance with prolonging heating time, however the absorbance of unheated solution had no obvious change (Figure 1c and Figure S1e,f (Supporting Information)). It was noted that the color of polyphenol solution darkening and UV absorption increasing in oxidation conditions usually imply the generation of species with higher molecular weight and polymerization of polyphenols.[16] Then, the influence of oxygen in the heating polymerization process was investigated by employing deoxygenated GA solution and deuterium oxide as solvent, respectively. For deoxygenated solution, the UV absorbance at 350 nm did not change significantly even after 12 h of consecutive heating. However, the absorbance of the same sample in presence of oxygen has increased by 6 times after 12 h heating compared with deoxygenated solution (Figure 1d). In addition, the introduction of deuterium oxide, known as a singlet oxygen half-life prolonger,[17] significantly increased the solution absorbance after heating (Figure 1e). These results demonstrated the existence of oxygen and reactive oxygen species (ROS) were essential for the heating polymerization of natural polyphenols and elevation of ROS concentration could promote the polymerization progress.

In order to detailly understand the chemical structure of GA NDs, we first employed Fourier transform infrared spectroscopy (FTIR) to confirm the chemical bonds (Figure S1g, Supporting Information). It was found that the intensity of multiple peaks of GA NDs in the range from 750 to 1620 cm^{-1} decreased significantly, which originated from benzene ring C—H, aromatic ester group, phenolic group, and benzene ring, and such reduction suggested the polymerization of GA.[18] The phenolic group signal at δ 9.16 and 8.81 ppm and carboxyl group signal at δ 12.74 ppm in ^{1}H nuclear magnetic resonance (NMR) spectrum of GA NDs disappeared (Figure 1f), which might be attributed by the replacement of hydrogen and/or coordination and complexation between hydroxyl and carboxyl groups. X-ray photoelectron spectroscopy (XPS) analysis of GA NDs and small molecule further proved the degree of oxidation rise after polymerization (Figure 1g,h). However, electrospray ionization mass spectrometry (ESI-MS) results of the reaction mixture implied the presence of supramolecular assembly structure during the reaction process (Figure S2a, Supporting Information).[19] To avoid the shielding effect of GA monomer assembly at high concentration, we examined ESI-MS results of GA solution at a relatively low concentration. It was found that some peaks of species with higher molecular weight in the spectra and the corresponding oligomer structures were depicted in Figure S2b (Supporting Information), which were also proposed in previous literatures.[16a,20] Yet, the proportion of four peaks in C 1s of NDs and monomer did not change remarkably. Together with the results from ESI-MS of reaction mixture and transmission electron microscopy (TEM) images with high resolution, we speculated that physical supramolecular assembly also contributed to the formation of natural polyphenolic NDs. Furthermore, the benzene ring

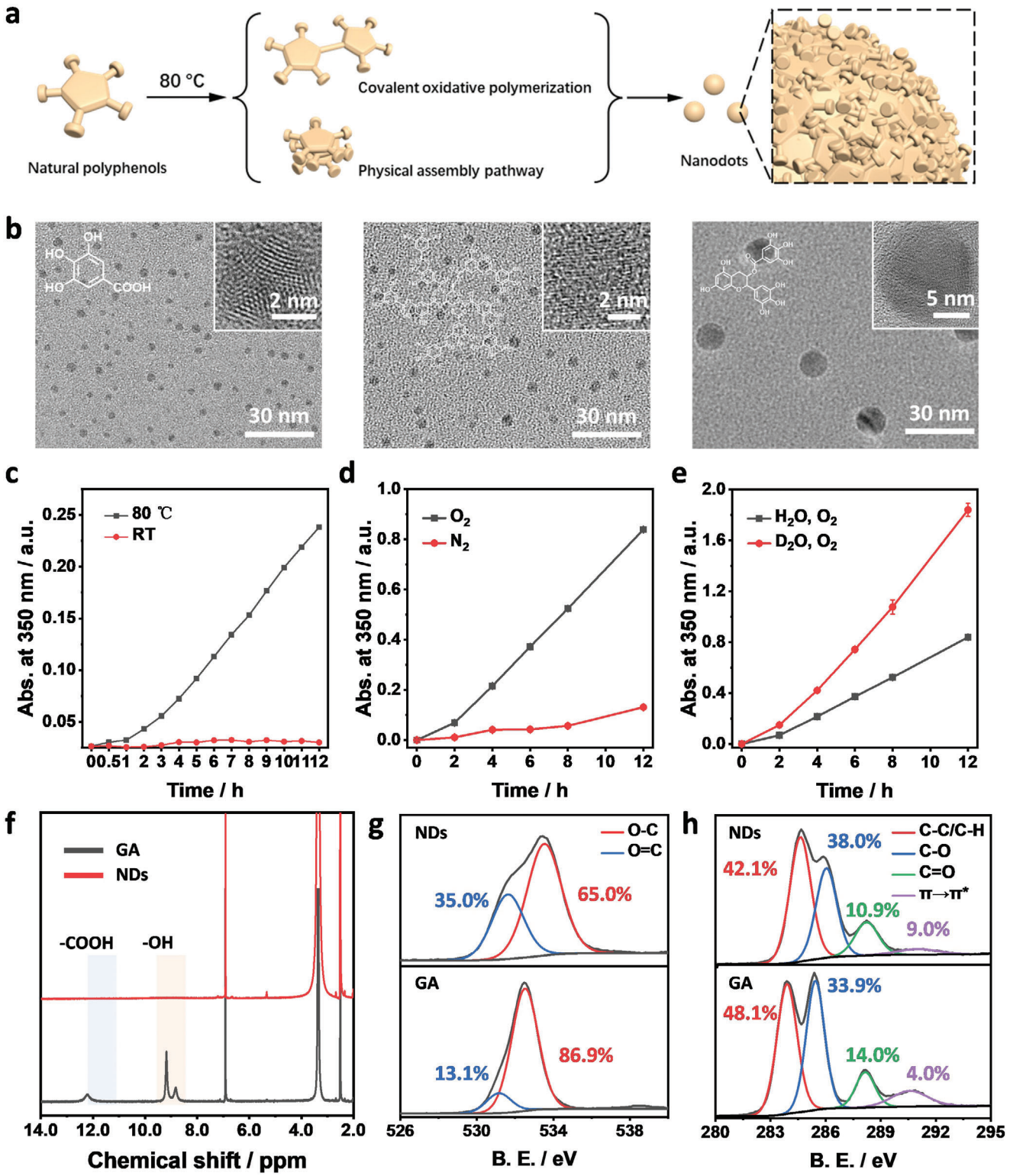

Figure 1. a) Schematic of the natural polyphenolic ND synthesis through covalent oxidative polymerization and physical assembly pathway. b) TEM images of natural polyphenolic NDs derived from gallic acid (GA), tannic acid (TA), and epigallocatechin gallate (EGCG), respectively (inset is selected NDs with high resolution). c) UV absorbance at 350 nm of GA solution as a function of time. d) UV absorbance at 350 nm of GA solution after deoxygenation with N_2 (red) or not (gray) for solutions heated. e) UV absorbance at 350 nm of GA solution in deionized water (gray) and deuterium oxide (red) heated. f) ^{1}H NMR spectra of GA (gray) and GA NDs (red). g) High-resolution XPS spectra of O 1s regions of GA NDs (top) and GA (down). h) High-resolution XPS spectra of C 1s regions of GA NDs (top) and GA (down).

C—H signal at δ 6.93 ppm in ^{1}H NMR spectrum of GA NDs diminished rather than disappeared (Figure 1f), which elucidated that hydroxyl, carboxyl, and phenolic groups participated in the formation of the NDs. Also, the absorption of typical peaks (3000–3500 cm^{-1}) in FTIR decreased and the O—H stretching vibration at 3496 cm^{-1} shifted to 3448 cm^{-1}, indicating the presence of hydrogen bond in the NDs (Figure S1g, Supporting Information). Consequently, the overall mechanism for natural polyphenolic ND formation might consist of two pathways: covalent oxidative polymerization and physical assembly (Figure S3, Supporting Information), which occurred in parallel.

2.2. NDs Inhibiting and Disaggregating A$\beta_{1\text{-}42}$ Fibrillation

Following, we tested the capacity of GA NDs to inhibit A$\beta_{1\text{-}42}$ fibrillation and disaggregated preformed fibrils (**Figure 2**a). As shown in Figure 2b, A$\beta_{1\text{-}42}$ would form aggregates when incubated alone as assessed by thioflavin-T (ThT) fluorescence intensity (Figure 2b). By contrast, the existence of GA NDs in A$\beta_{1\text{-}42}$ solution restrained the increase of ThT fluorescence intensity, indicating that the GA NDs can prevent A$\beta_{1\text{-}42}$ fibrillation. TEM images of the products also showed that A$\beta_{1\text{-}42}$ monomers were transformed into larger aggregates while some fragmented clusters can be found in the A$\beta_{1\text{-}42}$ solution when incubated with GA NDs at the end point (Figure 2c). Moreover, GA NDs also triggered the dissociation of preformed A$\beta_{1\text{-}42}$ fibrils and the ThT fluorescence intensity decreased rapidly after adding the NDs for 4 h (Figure 2d). Especially, the presence of A$\beta_{1\text{-}42}$ corona around the NDs can be clearly observed (Figure 2e), which testified that GA NDs could alter the aggregation process of A$\beta_{1\text{-}42}$ monomer, and the spherical clusters decreased the A$\beta_{1\text{-}42}$ concentration in solution. The same assessments were also monitored by dynamic light scattering (DLS) measurements (Figure 2f). More importantly, the GA NDs showed stronger ability to inhibit the A$\beta_{1\text{-}42}$ fibril formation compared with GA monomers (Figure 2g), which might be attributed by the multivalent binding of NDs with A$\beta_{1\text{-}42}$ fibrils.[21] It was considered that there were numerous catechol and quinone groups on the NDs surface, where the catechol groups can form H-bonds with Glu, Ala, and Asp residues of A$\beta_{1\text{-}42}$ fibrils, and the quinone groups tended to react with free amines within the A$\beta_{1\text{-}42}$ fibril via Schiff bases.[12a] These effects benefited the intervention into A$\beta_{1\text{-}42}$ fibrils and enlarged the spacing between Aβ strands, further damaging the β-sheet structure stability of fibrils. Therefore, every nanodot could generate multivalent binding with A$\beta_{1\text{-}42}$ fibrils, and provide enhanced binding interaction of NDs with fibrils compared to monovalent binding formula for GA monomer. In order to further analyze the secondary structure change of A$\beta_{1\text{-}42}$ fibrils, circular dichroism (CD) spectra were employed and the secondary structure analyses were determined by BeStSel program (Figure 2h).[22] After incubating with GA NDs, the secondary structure significantly changed with the β-sheet component reducing from 76.3% to 25.7%, and α-helix components increasing to 52.0% (Figure 2i). Collectively, GA NDs can suppress A$\beta_{1\text{-}42}$ fibrillation and disaggregate A$\beta_{1\text{-}42}$ fibrils, and the multiple binding presentations in the NDs enhanced the ability of the NDs to remodel Aβ fibril structures.

2.3. Biocompatibility, Neuroprotection Effects, and BBB Crossing Ability of NDs

Prior to assessing the neuroprotection effects of GA NDs in vitro, the biocompatibility of the NDs was investigated by methyl thiazolyl tetrazolium (MTT), AlamarBlue, and Cell Counting Kit-8 (CCK-8) assays (**Figure 3**a and Figure S4a (Supporting Information)). The cell viability remained ≈90% even with the ND concentration reaching 100 μg mL^{-1}, while the cell viability incubated with 25 μg mL^{-1} GA monomer had 65% left, suggesting the great biocompatibility of GA NDs. The hemolytic test further confirmed the remarkable blood compatibility (Figure 3b). Then, we assessed the influence of the NDs on Aβ-induced cytotoxicity. It could be found that the viability of SH-SY5Y cells significantly decreased to ≈30% after incubating with A$\beta_{1\text{-}42}$ for 24 h (Figure 3c). However, the coincubation with A$\beta_{1\text{-}42}$ monomer and GA NDs effectively increased the viability to ≈35% (25 μg mL^{-1}) and 50% (50 μg mL^{-1}), respectively, which might be contributed by the enhanced inhibiting effect on A$\beta_{1\text{-}42}$ fibril formation of GA NDs. To visualize the effect, the cells were stained with ThT and bright green fluorescence was observed when cells were incubated with A$\beta_{1\text{-}42}$ alone, demonstrating the formation of A$\beta_{1\text{-}42}$ fibrils around the cells (Figure 3d,e). Notably, the ThT fluorescence intensity decreased evidently after coincubation with GA NDs. Based on the excellent performance of GA NDs on alleviating Aβ-induced cytotoxicity and radical scavenging ability (Figure S4b,c, Supporting Information), the intracellular ROS levels induced by Aβ were further assessed. As displayed in Figure 3f, strong green fluorescence of A$\beta_{1\text{-}42}$-treated cells was captured while untreated cells possessed almost no fluorescence signal (Figure 3g). By contrast, the fluorescence intensity of the cells treated with GA NDs nearly disappeared, indicating that the intracellular ROS level declined sharply. To further verify the cytoprotective effect of NDs on moderating oxidative stress, the depolarization of mitochondrial membranes of cells was evaluated by JC-1 assay. It was perceived that the A$\beta_{1\text{-}42}$-treated cells manifested enhanced green fluorescence compared with control group, standing for lower mitochondrial membrane potential due to mitochondrial damage (Figure 3h). Yet, the mitochondrial membrane potential of cells was restored when cotreated with GA NDs as forecasted by the decreased green fluorescence (Figure S4d, Supporting Information). These results suggested that GA NDs could prevent A$\beta_{1\text{-}42}$ fibrillation in vitro and protect cells from the damages originated from A$\beta_{1\text{-}42}$ fibrils and A$\beta_{1\text{-}42}$-induced ROS.

Considering the intractable BBB is the main barrier to delivery drugs to brain for the brain-related diseases therapy, a normal transwell model was carried out to evaluate the BBB penetration efficiency of GA NDs (Figure S5a,b, Supporting Information), which was calculated to be 22.98 ± 3.63%. We further evaluate the inhibitory effects of GA NDs on A$\beta_{1\text{-}42}$ fibril formation and ROS generation in BBB model. It was illustrated that GA NDs could diminish the formation of A$\beta_{1\text{-}42}$ fibrils around the cells in lower chamber, as well as ROS level in cells (Figure S5c–f, Supporting Information). Subsequently, we examined the biodistribution and brain accumulation of GA NDs in healthy mice. The NDs were labeled with Cy5 dyes for in vivo tracking. It was revealed that the NDs could cross BBB and reach the brain area quickly after 0.5 h injection (Figure S6, Supporting Information). Despite high fluorescence level detected in main organs,

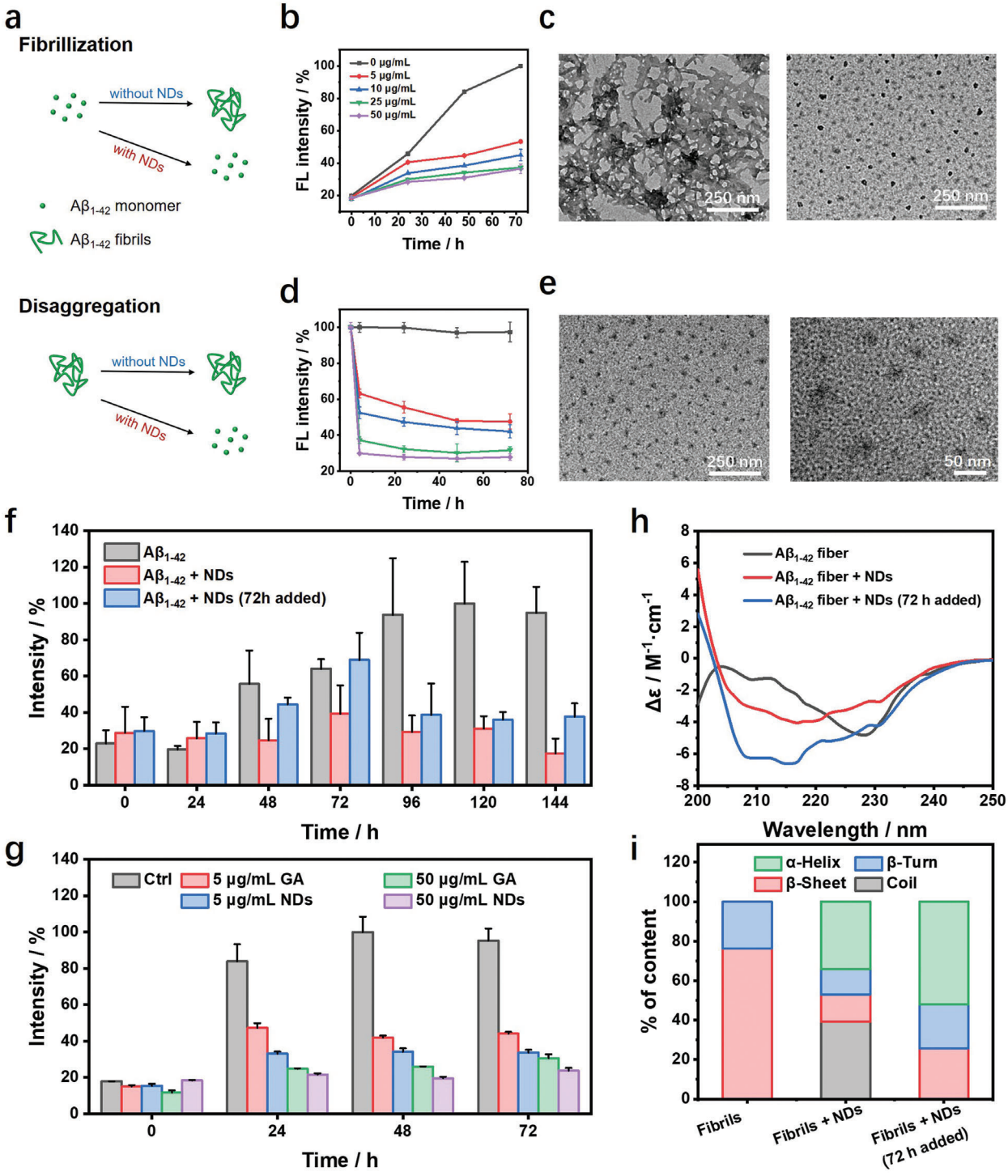

Figure 2. a) Schematic representation of inhibition and disaggregation of the A$\beta_{1\text{-}42}$ fibrillation via GA NDs with different concentrations (A$\beta_{1\text{-}42}$ concentration: 25 μM). b) A$\beta_{1\text{-}42}$ fibrillation process monitored by ThT fluorescence in the absence and present of GA NDs. c) TEM images of A$\beta_{1\text{-}42}$ monomer solution without GA NDs (left) and with GA NDs (right) after incubation for 72 h. d) Disaggregation of performed A$\beta_{1\text{-}42}$ fibrils monitored by ThT fluorescence in the absence and present of GA NDs. e) TEM images of performed A$\beta_{1\text{-}42}$ fibrils solution with GA NDs (50 μg mL^{-1}) after incubation for 72 h (left). The high-magnification TEM images (right) showed that A$\beta_{1\text{-}42}$ corona (white circle) can be observed around GA NDs (red circle). f) A$\beta_{1\text{-}42}$ fibrillation inhibition and disaggregation process monitored by DLS measurement in the absence and present of GA NDs (50 μg mL^{-1}). g) A$\beta_{1\text{-}42}$ fibrillation inhibition effects of GA monomer and GA NDs at the same concentration monitored by ThT fluorescence. Mean values and *p* values of (b, d, f, g) were listed in Table S1 (Supporting Information). h,i) CD spectra and secondary structure analysis of A$\beta_{1\text{-}42}$ monomer solution without GA NDs (black) and with GA NDs (red) after incubation for 72 h, and performed A$\beta_{1\text{-}42}$ fibril solution with GA NDs (50 μg mL^{-1}) after incubation for another 72 h (blue) by BeStSel program.

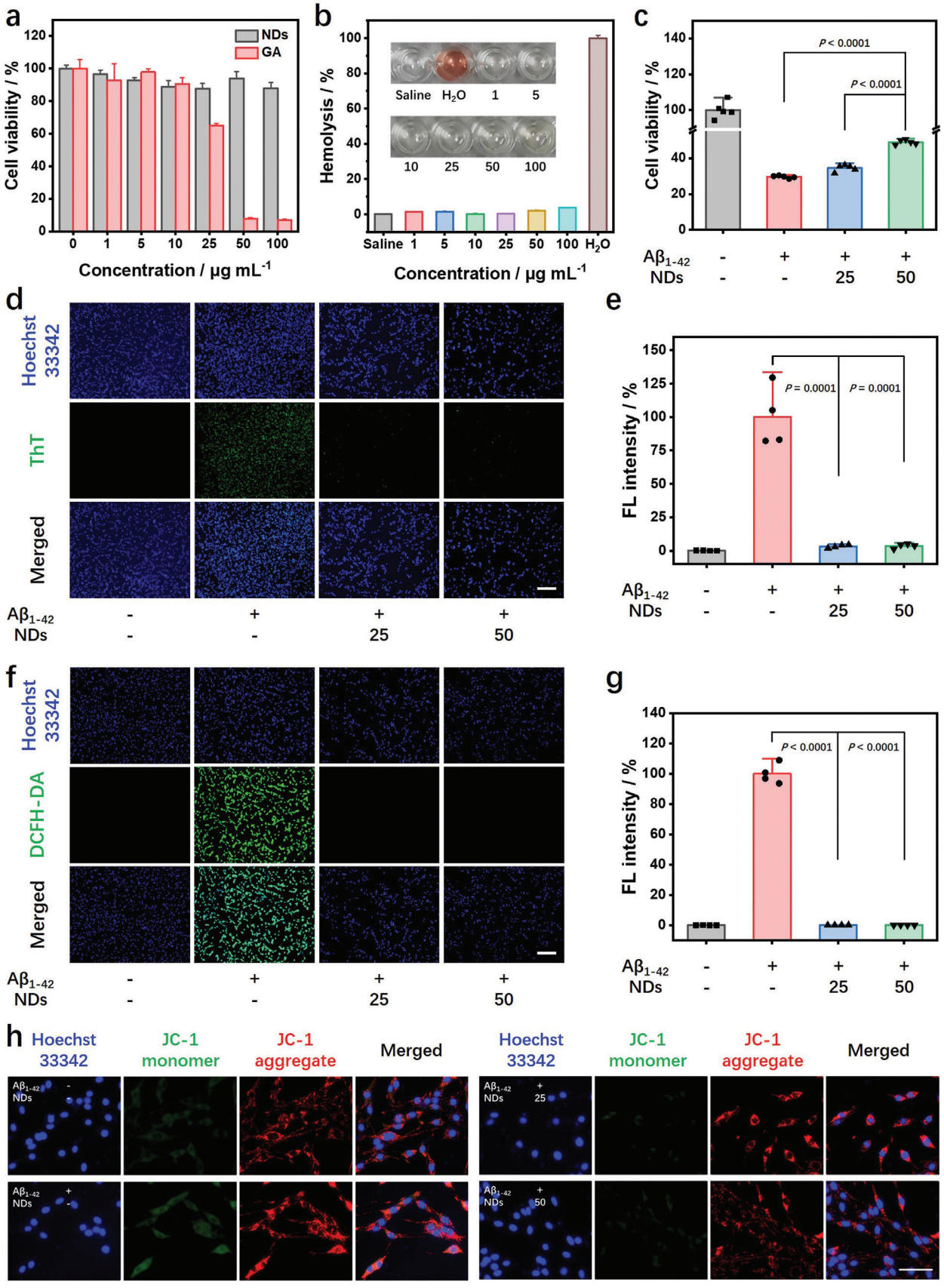

the brain fluorescence remained even after 24 h postinjection. Anyway, the results mentioned above proved that GA NDs could pass through BBB and achieve high brain accumulation, which greatly assisted in the treatment of AD.

2.4. Behavioral Evaluation of NDs in Transgenic Mice

Encouraged by the prominent neuroprotection effects, BBB penetration ability, colloid stability, and pharmacokinetics (Figure S7, Supporting Information), we further applied GA NDs on APP/PS1 transgenic mice to assess the therapeutic effect on AD. According to the schedule (**Figure 4**a), APP/PS1 mice were randomly grouped and intravenously injected with different preparations. Wild-type (WT) mice were employed to confirm the AD-relevant deficits in transgenic mice at baseline. After the last administration, behavioral experiments were performed to assess learning and memory ability of mice. In Morris water maze (MWM) training, APP/PS1 mice showed longer escape latency than WT mice (Figure S8a, Supporting Information). After the ND administering, escape latency of the mice was shortened, while the GA-treated mice exhibited longer escape latency than ND group, which was similar to that of APP/PS1 mice. On the testing day, the mice in APP/PS1 group showed poor and aimless searching strategy whereas the swimming paths of the ND-treated mice mainly revolved around the hidden platform (Figure 4b and Figure S8b (Supporting Information)). Notably, the mice administrated with GA monomer also showed indecisively swimming behavior, which was similar to APP/PS1 group. Moreover, the behavior analysis implicated that the treatment of GA NDs could effectively improve the learning ability and memory behavior with the same swimming speed, in terms of latency to reach the platform, number of platform crossing, and time in the targeting quadrant (Figure 4c–f). Furthermore, the memory impairment of the mice was investigated by Y-maze test. Compared with WT group, the spontaneous alternations of the mice in APP/PS1 group significantly decreased while the ND treatment improved the alternation near to WT level (Figure 4g,h and Figure S9 (Supporting Information)). Interestingly, the alternation of GA group was comparable to APP/PS1 group, which was in agreement with the results obtained in MWM test. These results stated that GA NDs were able to diminish cognitive and learning deficits in AD mice whereas GA monomer seemed to have few effects on cognitive and learning improvement.

2.5. Mechanism Analysis and Biosafety Assessment

It was known that the Aβ oligomer decomposed from Aβ plaques possessed higher neurotoxicity. To address this issue, the Aβ levels in brain and serum were determined by immunohistochemical staining, immunofluorescence staining, and enzyme-linked immunosorbent assay (ELISA). Compared with APP/PS1 mice, the level of Aβ visibly diminished both in brain and serum in the NDs-treated APP/PS1 mice (**Figure 5**a,b and Figure S10a (Supporting Information)). Notably, GA monomer caused a small quantity of Aβ plaque decrease and many residues of Aβ plaque were found in serum (Figure S10b, Supporting Information). These results suggested that GA NDs were able to not only disaggregate the preformed Aβ plaques in brain, but also promote the elimination of decomposed Aβ species. Subsequently, the levels of insulin-degrading enzyme (IDE) and neprilysin (NEP) that both relate to Aβ-degrading were calculated by western blotting (WB) assay. Surprisingly, the IDE level of APP/PS1 mice was higher compared with WT group and ND-treated mice contained the level near to that of WT mice, while the results of NEP showed the similar trend to that of IDE (Figure 5c and Figure S10c (Supporting Information)), which might be attributed by the response to Aβ load in APP/PS1 animals and the compensation action of NDs.[23] In other words, the NDs could resolve Aβ plaques and trimmed the demand for generation of IDE, which further inferred that the NDs possessed strong ability to deconstruct Aβ plaques.

The effective disaggregation of Aβ plaques could prevent nerve cells from Aβ-induced ROS damage. As expected, the ROS level showed as red fluorescence signal in APP/PS1 mice was much higher than that of WT mice, while plain relief of oxidative stress was illustrated after the NDs treatment (Figure 5d). However, the administration of GA monomer was ineffective, which agreed with the malonaldehyde (MDA) levels (Figure 5e). We further explored the nuclear-factor (erythroid-derived 2)-like 2 (Nrf2)-mediated signaling pathway by WB analysis, which was activated to protect cells from damages when suffering oxidative stress. Interestingly, Nrf2 of WT mice was kept in resting state while the level increased in APP/PS1 mice (Figure 5f). The expression of Nrf2 recovered to low level after treatment of NDs, suggesting that the oxidative stress in the microenvironment was normalized by NDs. The expression levels of downstream antioxidant proteins activated by Nrf2 including GCLM and NQO-1 were similar to that in Nrf2 testing (Figure 5g). Moreover, the microglial polarization was enthusiastically involved in the microenvironment modulation of AD, and normalization of microglial activation (M1 to the M2 state) would benefit the restoration of brain.[24] The representative images costained with CD206 (M2 microglia marker), CD86 (M1 microglia marker), and Iba-1 (microglia marker) indicated that NDs gained increased colocalization of CD206 and Iba-1 in the cortex of APP/PS1 mice while the colocalization of CD86 and Iba-1 reduced (Figure 5h). Inflammation-related cytokine secretion was further identified by real-time quantitative polymerase chain reaction (qRT-PCR). It was demonstrated that NDs were capable of downregulating proinflammatory cytokines such as TNF-α and IL-6 expression and increasing anti-inflammatory cytokine expression including

Figure 3. a) Viability of SH-SY5Y cells incubated with different concentrations of GA monomer and GA NDs. b) Hemolysis results of GA NDs in different concentrations. c) Viability of SH-SY5Y cells incubated with $A\beta_{1\text{-}42}$ (25 μM) alone or $A\beta_{1\text{-}42}$ with GA NDs (25 or 50 μg mL^{-1}) for 24 h. The viabilities were measured by MTT assay. d) Fluorescence images and e) fluorescence intensity stained by ThT of $A\beta_{1\text{-}42}$ (25 μM) fibrillation in SH-SY5Y cells after 24 h incubation with GA NDs (25 or 50 μg mL^{-1}). The fluorescence intensity was quantified by Image J according to fluorescence images. Scale bar: 20 μm. f) Fluorescence images and g) fluorescence intensity of intracellular ROS level stained by DCFH-DA. The fluorescence intensity was quantified by Image J according to fluorescence images. Scale bar: 20 μm. h) Protection effect of GA NDs on mitochondrial membrane integrity of SH-SY5Y cells stained by JC-1. Scale bar: 5 μm. Data presented as mean ± SD, $n = 4$.

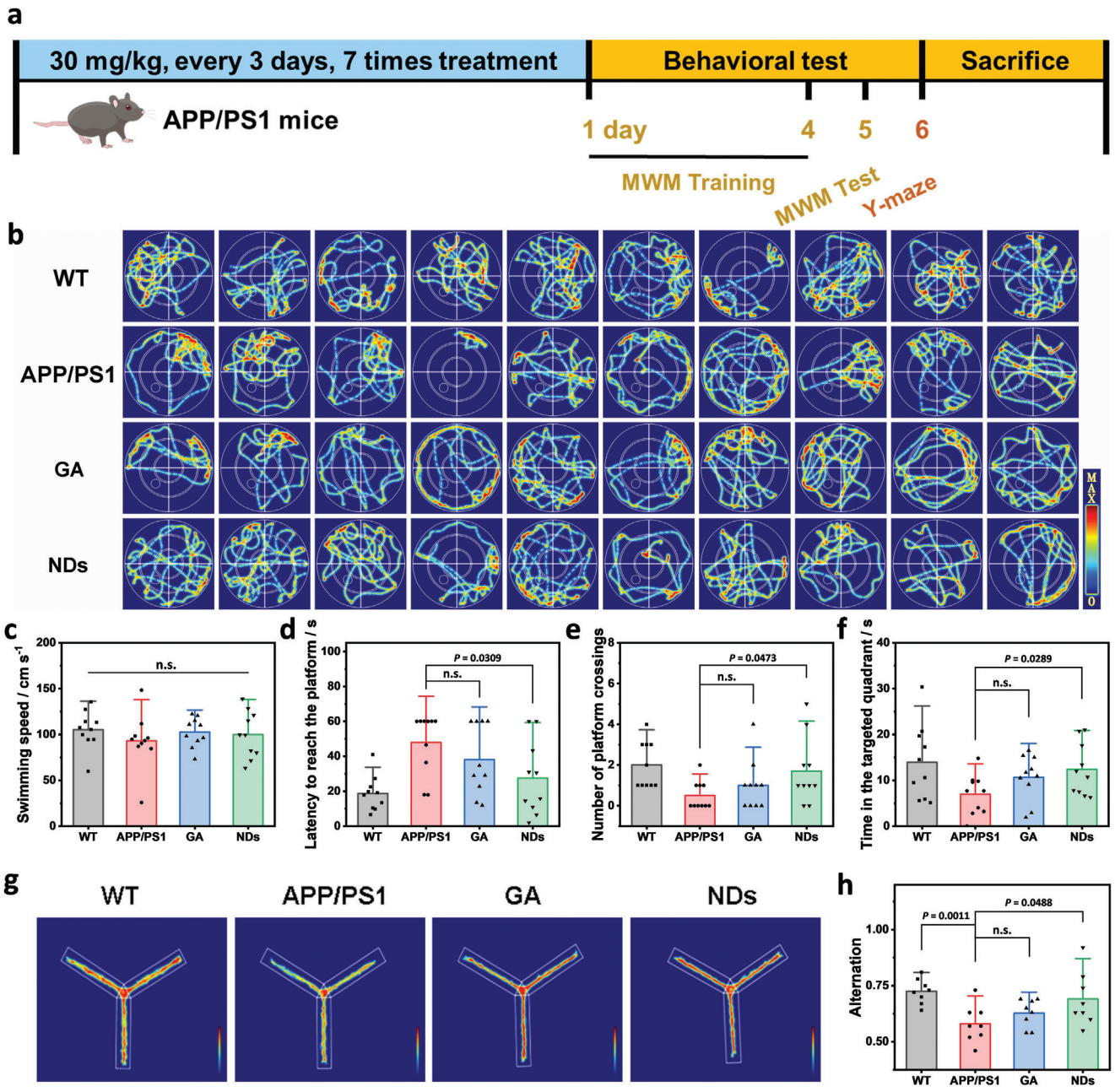

Figure 4. a) Timeline of animal experiment. WT mice were treated with 5% glucose (WT group) and APP/PS1 transgenic mice were treated with GA monomer (GA group, 30 mg kg^{-1}), GA NDs (NDs group, 30 mg kg^{-1}), or 5% glucose (APP/PS1 group) by tail intravenous injection every 3 days for 7 times treatment. The mice were subjected to MWM and Y-maze tests for memory and study evaluation. Then, the mice were sacrificed and relevant samples were collected for further assessments. b) Swimming path heatmaps of mice in MWM test. c) The swimming speed, d) the time to reach the targeted platform, e) the number of platform crossing, and f) the time staying in the targeted quadrant in different groups after treatment. g) Representative heatmap of Y-maze trials. h) Spontaneous alternation in Y-maze test. Data presented as mean ± SD, $n = 10$ mice per group.

TGF-β, IL-2, and IL-10 (Figure 5i and Figure S10d (Supporting Information)). These results suggested that the NDs could disaggregate Aβ plaques, scavenge intracellular ROS, and influence microglial polarization to normalize the microenvironment in the AD brain.

Furthermore, the neuron damage was estimated by neuronal marker NeuN. As shown in Figure 5j, the decrease of red fluorescence signal in NeuN staining, exhibiting the neuron density in hippocampus (HPC), showed that neurons of APP/PS1 mice were damaged. After NDs administration, the neuron density obviously increased while GA monomer failed to rescue neuron density. Similar results also can be obtained by hematoxylin-eosin (H&E) staining and Nissl staining (Figure 5k and Figure S10e (Supporting Information)). Prominently, distinct nuclear shrinking and damages were detected in CA1 and CA3 areas, related with the memory and study, of APP/PS1 mice. On the contrary,

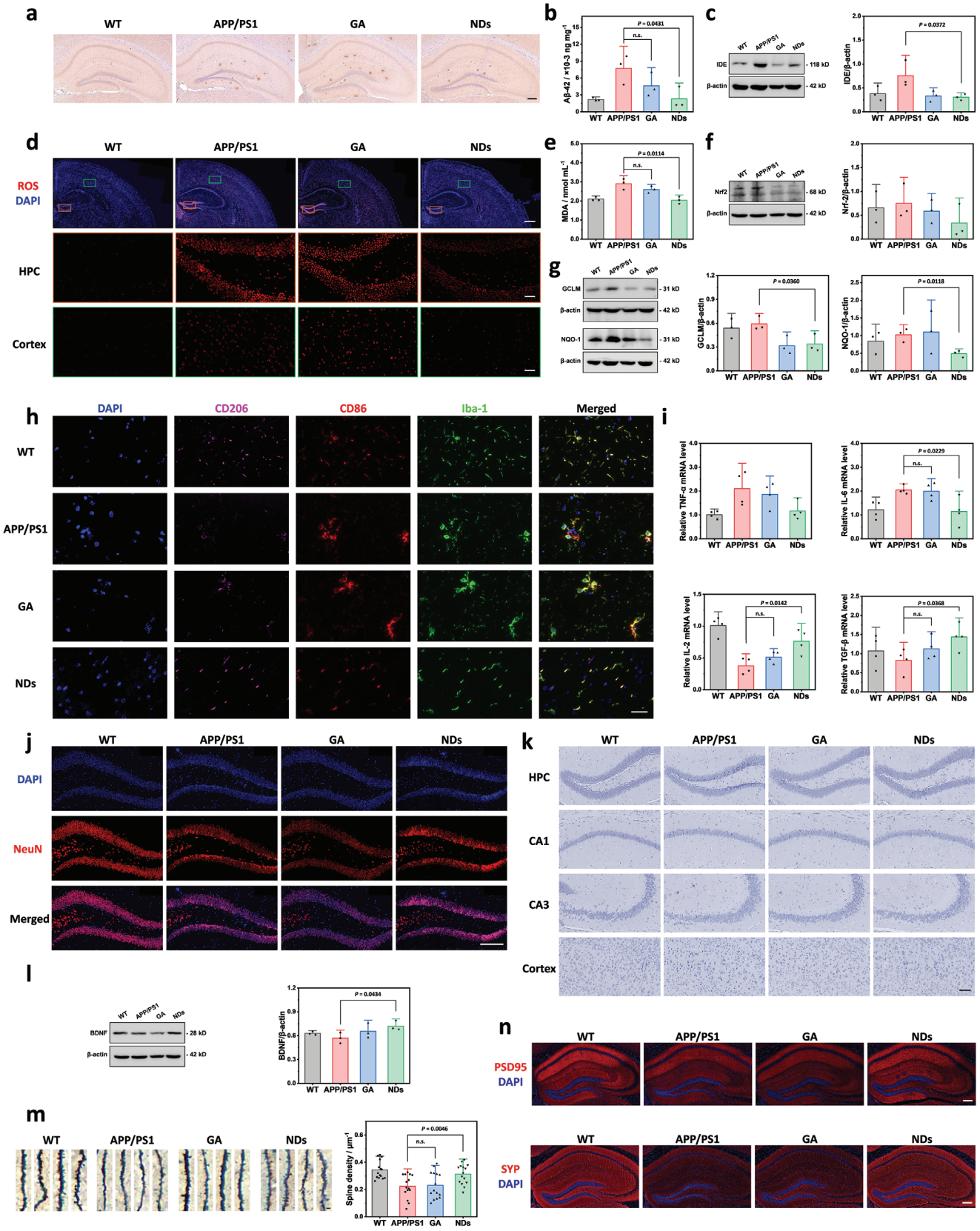

Figure 5. a) Immunohistochemical staining of Aβ plaques in the hippocampus (HPC) of APP/PS1 transgenic mice treated with GA monomer and NDs. Scale bar: 200 μm. b) Aβ level in brain determined by ELISA. c) Representative WB bands and statistical results of IDE. d) ROS level results in HPC and

the treatment of NDs mitigated the damages of neurocyte, which was further evidenced by the effective rise of brain-derived neurotrophic factor (BDNF) level based on WB results (Figure 5l). Besides, the morphologies of neurons were observed by Golgi–Cox staining based on the metal infiltration (Figure 5m), which was the structural basis of learning ability and memory formation. The dendritic spines in APP/PS1 group clearly decreased and the ND treatment rescued the depressed dendritic spines. However, GA possessed little effect on improving dendritic spine density in APP/PS1 mice. The synaptic deficit was further studied by evaluating the level of postsynaptic density protein 95 (PSD95) and synaptophysin (SYP), which was bound up with synaptic plasticity and cognitive ability. Immunofluorescence staining results showed higher fluorescence intensity in APP/PS1 mice after NDs treatment (Figure 5n), indicating that NDs were able to improve the expressions of PSD95 and SYP of APP/PS1 mice.

To further clarify the therapeutic mechanism of NDs, the transcriptomic analysis of mice brains was performed. The heatmap plot consisted of the differentially expressed genes (DEGs) between APP/PS1 and NDs groups (**Figure 6**a). After the administration of NDs, the DEGs added up to 676 compared with APP/PS1 mice, where 319 transcripts were downregulated (blue) and 357 genes were upregulated (red) (Figure 6b). The number of DEGs in ND-treated group was much higher than that in GA-treated group. Also, cluster analysis of DEGs indicated that ND treatment possessed a greater impact on changing gene expression patterns than that of GA (Figure S11, Supporting Information). The Gene Ontology (GO) revealed the differential gene expression items in ND group mostly referring to nervous system development, synapse system, memory, and learning cognition such as generation of neurons, nervous system development, neuron projection, and synapse, which was significantly regulated (Figure 6c). Interestingly, the items related with metal ions binding were also enriched, which could profit the prevention of Aβ plaque deposition and microenvironment modulation. Among the regulated genes, the genes in favor of the cure of AD, for example, *Slc5a7* for acetylcholine synthesis, *Gpr139* for neuromodulation, *Zfhx3* for circadian rhythms regulation, *Serpinb1a* for inflammation control, *Col25a1* for Aβ fibrillization inhibition, and *Eif5a2* for alleviating cell senescence, were remarkably upregulated. It has been well documented that cholinergic system possesses positive effects on brain homeostasis and plasticity,[25] and circadian rhythm management could adjust the Aβ fibrillization via chronotherapy for AD symptom relaxation (Figure 6d).[26] Besides, the adverse genes such as *Dkkl1*, *Crhbp*, and *Rtn4rl2* were notably downregulated. The decrease of *Dkkl1*, a unique *Dkk3*-related gene, was able to reduced apoptosis and increased neurogenesis,[27] and *Crhbp* could bind and inactivate corticotropin releasing hormone (CRH), where the CRH deficits conduces to cognitive impairment.[28] Additionally, *Rtn4rl2* could restrict the dendritic spine formation and growth during brain development.[29] Kyoto Encyclopedia of Genes and Genomes (KEGG) further elucidated the most significantly enriched signaling pathways related to AD (Figure 6e). Neuroactive ligand–receptor interaction, one of the most significantly enriched pathways related with AD, answers for the process regulation of neuronal communication, which was remarkably considerable for learning and memory.[30] Synaptic degeneration related pathways, such as calcium signaling pathway, Wnt signaling pathway, cholinergic synapse, and synaptic vesicle cycle, have been reported to be associated with cognitive impairment in AD, and the mitigation or stop of synaptic loss would benefit the cognitive rescue,[31] also being enriched. The other pathways were directly and/or indirectly associated with AD, which was targeted to profit AD patients.[32] Taking together, it was considered that the therapeutic effect of NDs on AD was on account of regulating multiple signaling pathways.

Finally, we evaluated the systemic toxicity of GA NDs. During the therapy process, there was no noticeable change in body weight among the groups and few pathological abnormalities were noted in major organs with H&E staining after sacrificing (Figure S12a,b, Supporting Information). The systemic responses to NDs were further assessed by routine blood parameters and chemistry, which revealed that the various indicators remained in the normal range and were consistent with the WT group (Figure S12c,d, Supporting Information). In short, the NDs at the given dosage in this study held good biocompatibility and were promising for clinical development.

3. Conclusion

In this work, we demonstrated an efficient and simple method to synthesize natural polyphenolic NDs for AD therapy by heating the monomer solution, which was dominated by covalent oxidative polymerization and physical assembly. The resulting NDs featured enhanced inhibition and dissociation ability toward Aβ aggregates/fibrils, as well as reducing Aβ-induced toxicity and promoting the clearance of Aβ species. Combined with the BBB permeating ability, the NDs showed unique therapeutic effects in transgenic AD mice. It is anticipated that the exploration of natural polyphenolic NDs would open new venues for clinical drug development for protein misfolding and aggregation-related neurodegenerative diseases.

4. Experimental Section

Chemicals and Materials: Gallic acid (98%) and tannic acid (95%) were purchased from Shanghai Aladdin Biochemical Technology Co., Ltd. Epigallocatechin gallate (98%) was obtained from Dasf Biotechnology

cortex stained with dihydroethidium (DHE). The orange box circled shows the HPC area, the green shows cortex area. Scale bar: 500 μm for the first line and 40 μm for others. e) MDA level results in serum. Representative WB bands and statistical results of f) Nrf2 and g) Nrf2-signaling-pathway-related proteins (GCLM and NQO-1). h) Immunostaining of CD86 (M1 marker, red), CD206 (M2 marker, purple), and Iba-1 (microglia marker, green) in cortex of APP/PS1 transgenic mice after administration of GA monomer and NDs. Scale bar: 30 μm. i) Expression of proinflammatory and anti-inflammatory cytokines in the brain after treatment. j) Immunostaining of NeuN positive cells in HPC of APP/PS1 transgenic mice. Scale bar: 50 μm. k) Nissl staining in different areas of APP/PS1 transgenic mice brain after treatment. Scale bar: 100 μm. l) Representative WB bands and statistical results of BDNF. m) Representative images of Golgi–Cox-stained dendrites in the HPC and the average values of dendritic spine numbers per micrometer. Scale bar: 2 μm. n) Immunofluorescence staining of PSD95 and SYP in HPC of APP/PS1 transgenic mice after treatment. Scale bar: 200 μm.

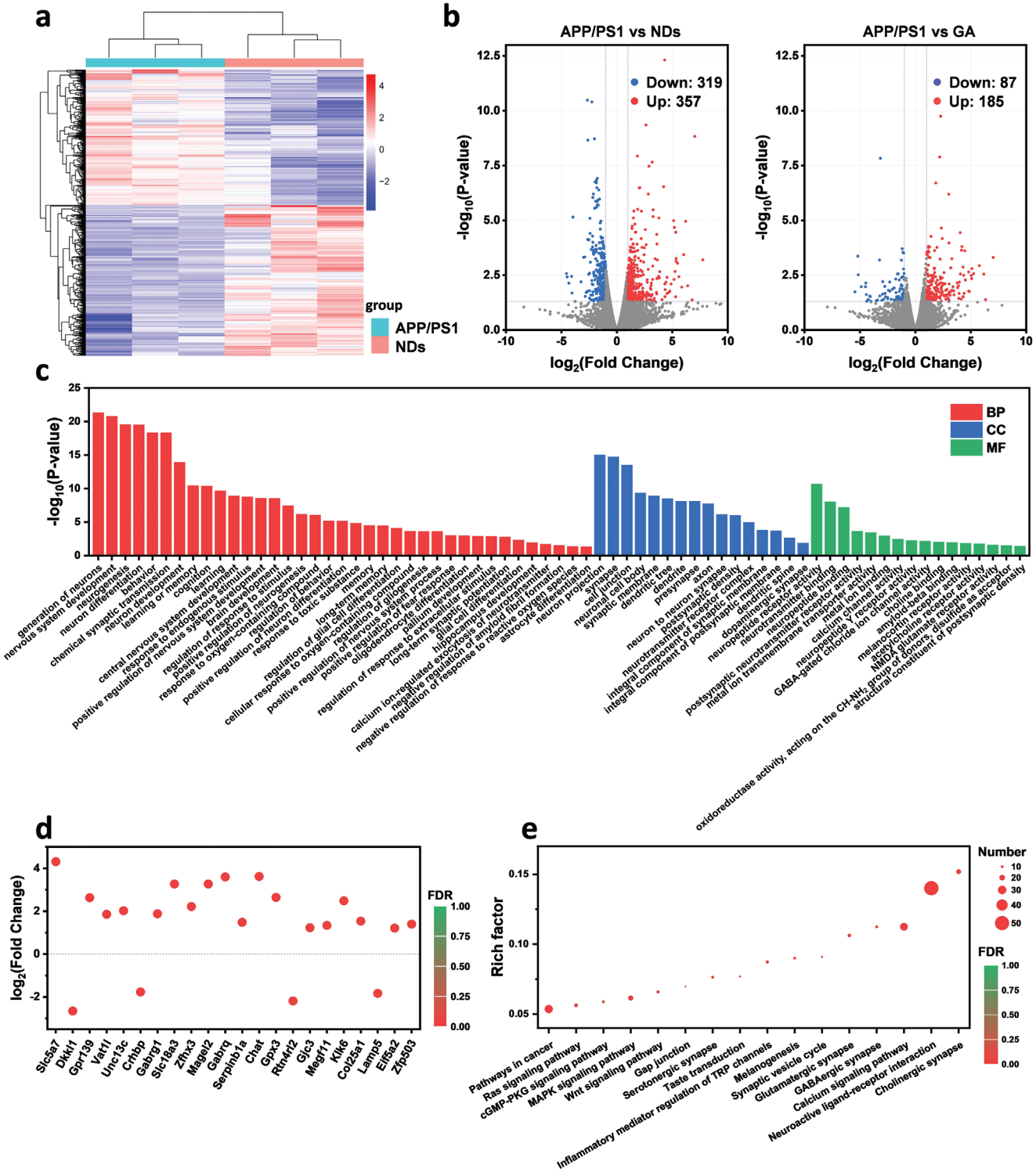

Figure 6. a) Heatmap plot of DEGs after NDs treatment compared with 5% glucose treatment. b) Quantitatively analyzed volcano plots of DEGs after NDs treatment (left) and GA treatment (right) compared with 5% glucose treatment ($p < 0.05$, |fold change| ≥ 2). c) GO enrichment analysis of DEGs exhibiting the involved pathways between APP/PS1 and NDs groups (BP: biological process, CC: cell component, and MF: molecular function). d) Representative DEGs between APP/PS1 and NDs groups ($p < 0.05$). e) KEGG enrichment analysis of enriched pathways between APP/PS1 and NDs groups ($p < 0.05$).

Co., Ltd. (Nanjing, China). Dimethyl sulfoxide (DMSO)-D_6 (99.8% D), D_2O (99.9% D), 1,1,1,3,3,3-hexafluoro-2-propanol (HFIP, 99%), ThT, 1,1-diphenyl-2-picrylhydrazyl (DPPH, 97%), 2,2′-azino-bis(3-ethylbenzothiazoline-6-sulfonic acid) diammonium salt (ABTS, 98%), MTT (99%), Hoechst 33342, 2′,7′-dichlorodihydrofluorescein diacetate (DCFH-DA, 97%), and JC-1 were purchased from Shanghai Titan Technology Co., Ltd. NaOH (99%) and $K_2S_2O_8$ (99%) were purchased from Chengdu Kelong Chemical Reagent Co. Ltd. A$\beta_{1\text{-}42}$ monomer (98%) was purchased from GL Biochem (Shanghai) Ltd. Cy5—NH_2 was purchased from New Research Biosciences Technology Co., Ltd.

Characterization: TEM images were performed on FEI transmission electron microscope (F20). The sample was stained with phosphotungstic acid. A Zetasizer NanoZS (Nano ZS ZEN 3690) was applied to measure zeta potentials and size distribution. The UV–vis absorption spectra were detected on a microspectrophotometer with a 1 cm quartz cell (PerkinElmer, Lambda 650). FTIR was conducted on a Fourier transform infrared spectrometer (Perkin-Elmer spectrum one B system) using KBr pellets. Fluorescence spectra were recorded on the F98 fluorescence spectrophotometer (Shanghai Lengguang Technology Co., Ltd.) with the excitation and emission slit width at 10 nm. The elemental composition of the sample surfaces was examined by X-ray photoelectron spectroscopy (PHI Quantera SXM spectrometer) using Al Kα X-ray radiation. ^{1}H NMR spectra were acquired in DMSO-D_6 using a Bruker AV III HD 400 MHz spectrometer. ESI-MS spectra were employed to analyze the possible chemical structures during the heating process by using Biosystems API 2000 with positive ion mode. For lower concentration solution, 0.2 mg mL^{-1} gallic acid solution without NaOH was used. CD spectra were collected over the wavelength range from 200 to 250 nm on J-1500-150 spectrometer (JASCO Corporation, Japan) and the secondary structure was analyzed using the BeStSel program (http://bestsel.elte.hu/).

Synthesis of Natural Polyphenolic NDs: For gallic acid, 200 mg monomer was dispersed in 10 mL water and 25 mg NaOH was added slowly to achieve complete dissolution. Then, the solution was heated at 80 °C for 12 h. Afterward, the solution was filtered through a 0.45 µm membrane filters (Beijing Balb Technology Co. Ltd.), then dialyzed with water through a dialysis bag (molecular weight cutoff 500 Da) for 48 h. Finally, the obtained purified products were freeze-dried and stored for further use. For tannic acid and epigallocatechin gallate, 200 mg monomer was dissolved in 10 mL water and the solution was heated at 80 °C for 12 h. Afterward, the solution was filtered through a 0.45 µm membrane filter (Beijing Balb Technology Co. Ltd.), then dialyzed with water through a dialysis bag (molecular weight cutoff 500 Da) for 48 h. Finally, the obtained purified products were freeze-dried and stored for further use.

UV–Vis Absorption Monitoring: Gallic acid solution (20 mg mL^{-1}, containing 2.5 mg mL^{-1} NaOH) was stored in room temperature (RT samples) and was heated at 80 °C (80 °C samples) for 12 h. At different time points, 200 µL reaction solution was added into 2000 µL water, which was used to record the UV–vis spectrum. For deoxygenated solutions, the solution went through three loops of freezing–vacuumizing–filling with N_2-thawing to remove oxygen. Then, the solution was heated at 80 °C for 12 h. At different time points, 200 µL reaction solution was added into 2000 µL water, which was used to record the UV–vis spectrum. For deuterium oxide medium, gallic acid solution in deuterium oxide was heated at 80 °C for 12 h. At different time points, 200 µL reaction solution was added into 2000 µL water, which was used to record the UV–vis spectrum.

A$\beta_{1\text{-}42}$ Sample Preparation: A$\beta_{1\text{-}42}$ powder was first dissolved with HFIP solvent (1 mg mL^{-1}) and the solution was sonicated in a water (25 °C, 30 min), which was stored at 4 °C overnight. Then, the solution solvent was evaporated under vacuum to remove HFIP. Prior to use, the A$\beta_{1\text{-}42}$ sample was dissolved in NaOH (20 mM) solution at a concentration of 500 µM and sonicated in water (10 min).

Fibrillization and Disaggregation of A$\beta_{1\text{-}42}$: For fibrillization, the A$\beta_{1\text{-}42}$ monomer solution (25 µM) diluted with phosphate-buffered saline (PBS) buffer (Gibco, containing additional 100 mM NaCl) was incubated with different concentrations of NDs. The mixed solution was placed in shaking bath at 37 °C with the speed of 120 rpm. For disaggregation, the A$\beta_{1\text{-}42}$ monomer solution (25 µM) diluted with PBS buffer (Gibco, containing 100 mM NaCl) was placed in shaking bath at 37 °C with the speed of 120 rpm for 72 h. Then, different concentrations of NDs were added for further 72 h. For ThT fluorescence assay, 70 µL of the sample solution was mixed with 1400 µL ThT solution (30 µM, PBS) and ThT fluorescence was measured (Ex = 440 nm, Em = 480 nm). ThT showed an obvious change of luminescence property when bounded to amyloid fibrils, where the excitation and emission maximums shifted from 380 and 445 to 450 and 482 nm, respectively. More importantly, the fluorescence intensity increased by several orders of magnitude, thereby avoiding the requirement of purification and allowing the real-time observation of fibrillation in solution. For DLS assay, 1.5 mL of sample solution was used to measure the hydrodynamic radius.

Radical Scavenging Testing: For DPPH assay, a fresh DPPH/ethanol (1 mM) solution was used for the measurements. The whole volume of testing solution was 3 mL, consisting of 300 µL DPPH solution and different concentration of NDs. After 30 min, 100 µL of testing solution was mixed with 2 mL water. The mixed solution was further used to record the UV–vis spectrum with the range of 450–650 nm. For ABTS assay, 0.1 mmol ABTS and 0.037 mmol $K_2S_2O_8$ were dissolved in 15 mL deionized water and the solution was under stirring in dark for 12 h. Then, 100 µL ABTS$^{\square+}$ solution was added into the deionized water containing different samples, and the total volume was 3 mL. After incubation for 30 min, the absorbance in the range from 600 to 800 nm was recorded.

Cell Culture: SH-SY5Y cells and bEnd.3 cells were cultured in Dulbecco's modified Eagle's medium (DMEM) supplemented with 10% fetal bovine serum and 100 units mL^{-1} penicillin and 100 µg mL^{-1} streptomycin in a humidified incubator with 5% CO_2 at 37 °C.

Cytotoxicity Test: For the cytotoxicity test, the cell viability was evaluated by MTT assay. SH-SY5Y cells were seeded in 96-well plate and incubated for 12 h (8000 cells per well). Then, the medium was removed and the cells were treated with new medium containing gallic acid or NDs at different concentrations. After another 24 h, the medium was removed and new medium containing MTT (0.5 mg mL^{-1}) was added. After another 4 h, the medium was removed and 150 µL DMSO was added. Then, the plate was oscillated for 10 min and the optical density (OD) value (490 nm) was recorded by microplate reader (BioTek, Epoch).

Hemolysis Test: The rat's blood was washed with saline water several times until the upper liquid was clear. Then, the red blood cells were resuspended in saline water at a concentration of 2%. 200 µL of the prepared red blood cell suspension was mixed with different concentrations of NDs, which was incubated at 37 °C for 2 h. Pure water and saline were used as the positive and negative samples. The mixture was then centrifuged (1500 rpm, 5 min) to determine the absorbance of the supernatant at 540 nm. The hemolysis was calculated by the following formula

$$\text{Hemolysis } (\%) = (\text{Ab}_s - \text{Ab}_{nc}/\text{Ab}_{pc} - \text{Ab}_{nc}) \times 100 \quad (1)$$

where Ab_s, Ab_{nc}, and Ab_{pc} were the absorbance of samples, negative and positive samples, respectively.

A$\beta_{1\text{-}42}$-Induced Cytotoxicity Test: For the cytotoxicity test, the cell viability was evaluated by MTT assay. SH-SY5Y cells were seeded in 96-well plate and incubated for 12 h (10 000 cells per well). Then, the medium was removed and the cells were treated with new medium containing A$\beta_{1\text{-}42}$ (25 µM) and NDs at different concentrations. After another 24 h, the medium was removed and 100 µL DMEM medium was added. The cell viability was measured by microplate reader (BioTek, Epoch) using standard MTT assay.

Fluorescence Images of ThT, ROS, and Mitochondrial Membrane Integrity Measurement: SH-SY5Y cells were seeded in 24-well plate and incubated for 12 h (50 000 cells per well). Then, the medium was removed and the cells were treated with new medium containing A$\beta_{1\text{-}42}$ (25 µM) and NDs at different concentrations for another 24 h. For ThT imaging, the cells were stained with ThT (40 µM, DMEM) for 30 min. Then, the cells were washed with medium 3 times and DMEM medium was added for fluorescence imaging. The fluorescence intensity was measured by Image J. For ROS imaging, the cells were stained with DCFH-DA (10 µM, DMEM) for 1 h. Then, the cells were washed with medium 3 times and DMEM was added for fluorescence imaging. The fluorescence intensity was measured by Image J. For mitochondrial membrane depolarization, mitochondrial

membrane potential was determined according to the manufacturer's instructions of the assay kits (JC-1, Beyotime Biotechnology). JC-1 yielded green fluorescence at low concentration due to low mitochondrial membrane potential, whereas turned to generate a red emission caused by the high mitochondrial membrane potential, which could be employed for the evaluation of polarization status.

Fluorescence Images of ThT and ROS in BBB Model: bEnd.3 cells were seeded in the upper chamber of transwell plate (24-well hanging insert) at the density of 50 000 cells per well. The medium was changed and the transendothelial electrical resistance (TEER) value was recorded every day. When TEER values reached about 180 Ω cm^{-2}, SH-SY5Y cells were seeded in the lower chamber (50 000 cells per well). For ThT, after 24 h, new medium containing NDs (50 μg mL^{-1}) was added in upper chamber, and another new medium containing A$\beta_{1\text{-}42}$ (25 μM) was added in lower chamber for another 24 h. The medium was removed and new medium containing ThT (40 μM, DMEM) was added in lower chamber for 30 min. Then, the cells were washed with medium 3 times and DMEM medium was added for fluorescence imaging. For ROS, after 24 h, new medium containing NDs (50 μg mL^{-1}) was added in upper chamber, and another new medium containing A$\beta_{1\text{-}42}$ (25 μM) or H_2O_2 (20 μM) was added in lower chamber for another 24 h. The medium was removed and new medium containing DCFH-DA (10 μM, DMEM) was added in lower chamber for 60 min. Then, the cells were washed with medium 3 times and DMEM medium was added for fluorescence imaging.

Animal: Male C57BL/6 mice (≈25 g) were purchased from Chengdu Dossy Experimental Animal Co., Ltd. Male APP/PS1 mice (≈25 g) were purchased from Changzhou Cavens Experimental Animal Co., Ltd. All animals were raised under standard housing conditions. All animal experiments were performed in accordance with the guidelines laid down and approved by the experimental animal management committee of Sichuan University. The assigned approval/accreditation number was KS2020420.

BBB Transportation Study: in vitro, bEnd.3 cells were seeded in the upper chamber of transwell plate (24-well hanging insert) at the density of 50 000 cells per well. The medium was changed and the TEER value was recorded every day. When TEER values were measured to be beyond 180 Ω cm^{-2}, the medium in the upper chamber of the well was replaced with NDs (50 μg mL^{-1}) dispersed in *N*-(2-hydroxyethyl)piperazine-29-(2-ethane-sulfonic acid) (HEPES) buffer (136 mM NaCl, 0.9 mM $CaCl_2$, 0.5 mM $MgCl_2$, 2.7 mM KCl, 1.5 mM KH_2PO_4, 10 mM NaH_2PO_4, 25 mM glucose, and 10 mM HEPES, pH 7.4) at 37 °C for 24 h. Then, the absorbance of the solution in the upper chamber was determined by UV–vis spectrometer. The transport ratio was calculated by the following formula

$$\text{Ratio}\ (\%) = (1 - A_s/A) \times 100 \quad (2)$$

where A_s was the absorbances at 320 nm of ND solution in the upper chamber after 24 h, and A was the absorbance at 320 nm of ND solution (HEPES buffer, 50 μg mL^{-1}).

in vivo, the NDs were first labeled with Cy5—NH_2. Briefly, 2 mg mL^{-1} NDs solution was mixed with Cy5—NH_2 (0.1 mg mL^{-1}). NaOH (1 M) was used to adjust the pH value of the mixed solution to ≈7. The mixed solution was stirred overnight. Then, the reaction solution was dialyzed against water through a dialysis bag (molecular weight cutoff 500 Da) protected from light by a black cover for 48 h. Finally, the obtained purified products were freeze-dried and stored for further use. The mice were randomly grouped and 100 μL of Cy5-labeled NPs (30 mg kg^{-1}) were administrated intravenously at the same concentration of Cy5. PBS-injected mice were used as control. After 0.5, 4, and 24 h postinjection, mice were anesthetized and imaged using the Lumina III Imaging System (PerkinElmer, USA). At 24 h, the mice were sacrificed and were perfused with PBS followed by 4% paraformaldehyde. Their major organs and brains were separated for *ex vivo* fluorescence imaging.

Pharmacokinetics Study: Male C57BL/6 mice were randomly divided into two groups (8 mice in each group), which were administrated intravenously with PBS or Cy5-labeled NPs (30 mg kg^{-1}). PBS-injected mice were used as control. After injection, the mice blood was obtained from retro-orbital sinus (clotting time > 0.5 h) at different time points. Then, the plasma was collected by centrifugation (3000 rpm for 10 min at 4 °C), of which the fluorescence intensity (Ex: 625 nm, Em: 685 nm) was further determined by fluorescence spectrophotometer. The standard curve of Cy5-labeled NPs with different concentrations in plasma was newly measured for quantitative analysis.

AD Treatment and Test Arrangements: 30 APP/PS1 mice were randomly divided into 3 groups (10 mice per group) and intravenously injected with 5% glucose (APP/PS1), GA (30 mg kg^{-1} in 5% glucose solution), and NDs (30 mg kg^{-1} in 5% glucose solution), respectively, every 3 days for 7 times. C57BL/6 mice were used as WT group and injected with 5% glucose. Body weight was recorded every 3 days. After the treatment was completed, behavioral experiments were carried out. After the behavioral experiments were completed, the mice were sacrificed for further mechanism experiences.

Morris Water Maze Test: The diameter of the water maze was 80 cm. The water temperature was maintained at 21 ± 1 °C. During the experiment, the pool was in a quiet test room with constant light, and four different geometric figures were placed on the wall of the pool, evenly dividing the pool into four quadrants. A circular platform was placed and fixed 1 cm underwater (10 cm in diameter) in the center of quadrant 3, and the position remained unchanged during training trials. A camera detector was set above the pool to track the trajectory of mice. Each mouse was trained 3 times a day for 4 consecutive days. The mice were released in the water facing wall of water maze from three different locations (1, 2, and 4 quadrants). If the mouse found the platform within 60 s and boarded the platform, the mouse was allowed to stay on the platform for 10 s and the latency was recorded. If failed, the mouse was guided to the platform and allowed to stay for 10 s, and the latency was recorded at 60 s. After 4 days of training trials, the platform was removed for space exploration experiments. Each mouse was allowed to swim freely for 60 s. Swimming speed, latency to reach the platform, number of platform crossing, and time in the targeted quadrant were recorded, respectively.

Y-Maze Test: The device was a plastic black maze with three arms: 30 cm long, 15 cm high, and 6 cm wide. The two adjacent arms met in the middle at an angle of 120°. During the experiment, the device was in a quiet test room with constant light, and a camera detection device was used to track the trajectory of the mice. The mice were placed from the end of one arm facing the end of the arm, allowing them to move freely in the maze for 5 min, and the trajectory of the mice was recorded from the time they were placed. When a mouse entered from one arm to the other, an entrance number was counted. When a mouse successively entered 3 different arms, an alternation number was counted. Before each trial, 75% ethanol solution and distilled water were used to clean the inside of the maze to remove any scent cues. The alternation was calculated by the following formula

$$\text{Alternation} = \text{alternation number}/\ (\text{entrance number} - 2) \quad (3)$$

Measurement of A$\beta_{1\text{-}42}$ Level by ELISA: For brain, the brain tissues were isolated from the mice and radioimmunoprecipitation assay buffer (RIPA) was added (200 μL buffer per 20 mg tissue). The mixture was homogenized by high-speed tissue grinder (Service bio, Wuhan, China) (60 Hz, 60 s). Then, the lysates were centrifuged at 4 °C (10 000 *g*, 15 min) and the supernatants were collected. The protein concentration of samples was determined by bicinchoninic acid (BCA) protein assay kit (Beyotime Biotechnology) and the A$\beta_{1\text{-}42}$ level of samples was determined by human A$\beta_{1\text{-}42}$ ELISA kit (Quanzhou Ruixin Biotechnology Co., LTD.) according to the manufacturer's instructions. For serum, the blood of mice was collected in centrifuge tube and stored for 2 h. Then, the blood was centrifuged at 4 °C (5000 rpm, 20 min). The serum (the supernatants) was collected. The A$\beta_{1\text{-}42}$ level and MDA level of samples were determined by human A$\beta_{1\text{-}42}$ ELISA kit (Quanzhou Ruixin Biotechnology Co., LTD.) according to the manufacturer's instructions.

Western Blot: For brain, the brain tissues were isolated from the mice and RIPA buffer was added (200 μL buffer per 20 mg tissue). The mixture was homogenized by high-speed tissue grinder (Service bio, Wuhan, China) (60 Hz, 60 s). Then, the lysates were centrifuged at 4 °C (10 000 *g*,

15 min) and the supernatants were collected. The protein solution was mixed with loading buffer, which was further boiled at 100 °C for 10 min. The samples were resolved to 10–12% sodium dodecyl sulfate - polyacrylamide gel electrophoresis (SDS-PAGE) with the dose of 40 µg per lane and transferred onto polyvinylidene fluoride membranes. Then, the membranes were blocked by 5% milk for 2 h at 37 °C and incubated with primary antibodies (1:500 for NEP and Nrf-2, 1:1000 for others) overnight at 4 °C. The following day, the membranes were incubated with the horseradish-peroxidase-conjugated secondary antibody (1:2000 for NEP and Nrf-2, 1:5000 for others) for 1.5 h at 37 °C. Finally, protein band intensities were detected by using the chemiluminescent imaging system and quantified by Image J software. All antibodies were purchased from ABclonal Technology Co., Ltd.

Mechanism Experiments and Toxicity Checking: The brain tissues were isolated and the cross-section of hippocampus and/or cortex were selected for immunohistochemistry and immunofluorescence staining, ROS staining, Nissl staining, Golgi–Cox staining, and H&E staining, respectively. In detail, the information of antibody for immunofluorescence staining was as follows: Aβ (abcam, ab201060, 1:200), CD86 (CST, 19589, 1:400), CD206 (CST, 24595, 1:200), Iba-1 (abcam, ab178846, 1:1000), PDS95 (abcam, ab238135, 1:50), SYP (abcam, ab32127, 1:100), NeuN (abcam, ab177487, 1:1000). The information of antibody for immunohistochemistry staining was as follows: Aβ (abcam, ab201060, 1:500). The blood of mice was collected for routine blood parameter and chemistry analysis. The major organs (heart, liver, spleen, lung, and kidney) were sectioned and stained with H&E, and the body weight was recorded to evaluate the cumulative toxicity of NPs in vivo.

Real-Time Quantitative RT-PCR Analysis: The total RNA from brain was extracted using animal total RNA isolation kit (Chengdu FOREGENE Biotechnology Co., Ltd.). cDNA was prepared by a reverse transcription system kit according to the manufacturer's instructions (Hieff III 1st Strand cDNA Synthesis SuperMix for qPCR (gDNA digester plus), Yeasen Biotechnology (Shanghai) Co., Ltd.). Real-time qPCR was performed by the Hieff qPCR SYBR Green Master Mix (Low Rox Plus) kit (Yeasen Biotechnology (Shanghai) Co., Ltd.) following the manufacturer's protocol. Expression levels were normalized to GAPDH and analyzed using the comparative cycle threshold ($F = 2^{-\Delta\Delta Ct}$) method. Primer sequences for qRT-PCR were listed as follows

IL 2-F 5′-ATGTACAGGATGCAACTCCTGTCTT-3′
IL 2-R 5′-GTCAGTGTTGAGATGATGCTTTGAC-3′
IL 6-F 5′-TAGTCCTTCCTACCCCAATTTCC-3′
IL-6-R 5′-TTGGTCCTTAGCCACTCCTTC-3′
IL 10-F 5′-GCTCTTACTGACTGGCATGAG-3′
IL 10-R 5′-CGCAGCTCTAGGAGCATGTG-3′
TNF α-F 5′-CGGGGTGATCGGTCCCCAAAG-3′
TNF α-R 5′-GGAGGGCGTTGGCGCGCTGG-3′
TGF β-F 5′-CAGTACAGCAAGGTCCTTGC-3′
TGF β-R 5′-ACGTAGTAGACGATGGGCAG-3′
GAPDH-F 5′-AGGTCGGTGTGAACGGATTTG-3′
GAPDH-R 5′-TGTAGACCATGTAGTTGAGGTCA-3′

Transcriptomic Analysis: After behavioral experiment, mice were sacrificed and their brains were isolated. The mice brains were rapidly transferred to liquid nitrogen after being cleaned with diethylpyrocarbonate water. Transcriptomics analysis of some mice brains was performed by the BioNovoGene (Suzhou, China).

Statistical Analysis: Statistical analysis was assessed by GraphPad Prism 8.0.2. All data were shown as mean ± standard deviation (SD). Statistical significance between two groups was analyzed by unpaired two-tailed Student's *t*-test (*$p < 0.05$, **$p < 0.01$, ***$p < 0.001$, ****$p < 0.0001$). Data were representative of three independent experiences at least.

Supporting Information

Supporting Information is available from the Wiley Online Library or from the author.

Acknowledgements

P.Y. and Q.H. contributed equally to this work. This work was financially supported by the National Natural Science Foundation of China (Grant No. 52173132), the Research and Development Program of Science and Technology Department of Sichuan Province (Grant No. 2022JDJQ0050).

Conflict of Interest

The authors declare no conflict of interest.

Data Availability Statement

The data that support the findings of this study are available from the corresponding author upon reasonable request.

Keywords

Alzheimer's disease, amyloid-β, nanodots, natural polyphenols

Received: August 18, 2023
Revised: November 7, 2023
Published online:

[1] a) D. J. Selkoe, *Science* **2021**, *373*, 624; b) H. Hampel, R. Au, S. Mattke, W. M. van der Flier, P. Aisen, L. Apostolova, C. Chen, M. Cho, S. De Santi, P. Gao, A. Iwata, R. Kurzman, A. J. Saykin, S. Teipel, B. Vellas, A. Vergallo, H. Wang, J. Cummings, *Nat. Aging* **2022**, *2*, 692; c) E. Nichols, J. D. Steinmetz, S. E. Vollset, K. Fukutaki, J. Chalek, F. Abd-Allah, A. Abdoli, A. Abualhasan, E. Abu-Gharbieh, T. T. Akram, H. Al Hamad, F. Alahdab, F. M. Alanezi, V. Alipour, S. Almustanyir, H. Amu, I. Ansari, J. Arabloo, T. Ashraf, T. Astell-Burt, G. Ayano, J. L. Ayuso-Mateos, A. A. Baig, A. Barnett, A. Barrow, B. T. Baune, Y. Béjot, W. M. M. Bezabhe, Y. M. Bezabih, A. S. Bhagavathula, et al., *Lancet Public Health* **2022**, *7*, e105.

[2] G. Livingston, J. Huntley, A. Sommerlad, D. Ames, C. Ballard, S. Banerjee, C. Brayne, A. Burns, J. Cohen-Mansfield, C. Cooper, S. G. Costafreda, A. Dias, N. Fox, L. N. Gitlin, R. Howard, H. C. Kales, M. Kivimäki, E. B. Larson, A. Ogunniyi, V. Orgeta, K. Ritchie, K. Rockwood, E. L. Sampson, Q. Samus, L. S. Schneider, G. Selbæk, L. Teri, N. Mukadam, *Lancet* **2020**, *396*, 413.

[3] a) P. C. Ke, M.-A. Sani, F. Ding, A. Kakinen, I. Javed, F. Separovic, T. P. Davis, R. Mezzenga, *Chem. Soc. Rev.* **2017**, *46*, 6492; b) S. J. C. Lee, E. Nam, H. J. Lee, M. G. Savelieff, M. H. Lim, *Chem. Soc. Rev.* **2017**, *46*, 310.

[4] a) E. Karran, B. De Strooper, *Nat. Rev. Drug Discovery* **2022**, *21*, 306; b) J. M. Long, D. M. Holtzman, *Cell* **2019**, *179*, 312.

[5] Q. Huang, C. Jiang, X. Xia, Y. Wang, C. Yan, X. Wang, T. Lei, X. Yang, W. Yang, G. Cheng, H. Gao, *Research* **2023**, *6*, 0180.

[6] L. Xu, Y. Ding, F. Ma, Y. Chen, G. Chen, L. Zhu, J. Long, R. Ma, Y. Liu, J. Liu, F. Huang, L. Shi, *Nano Today* **2022**, *43*, 101388.

[7] a) G. C. Alexander, D. S. Knopman, S. S. Emerson, B. Ovbiagele, R. J. Kryscio, J. S. Perlmutter, A. S. Kesselheim, *N. Engl. J. Med.* **2021**, *385*, 769; b) E. Karran, J. Hardy, *Ann. Neurol.* **2014**, *76*, 185.

[8] a) R. van der Kant, L. S. B. Goldstein, R. Ossenkoppele, *Nat. Rev. Neurosci.* **2020**, *21*, 21; b) R. Loera-Valencia, A. Cedazo-Minguez, P. A. Kenigsberg, G. Page, A. I. Duarte, P. Giusti, M. Zusso, P. Robert, G. B. Frisoni, A. Cattaneo, M. Zille, J. Boltze, N. Cartier, L. Buee, G. Johansson, B. Winblad, *J. Intern. Med.* **2019**, *286*, 398; c) P. Liu, T. Zhang, Q. Chen, C. Li, Y. Chu, Q. Guo, Y. Zhang, W. Zhou, H. Chen,

Z. Zhou, Y. Wang, Z. Zhao, Y. Luo, X. Li, H. Song, B. Su, C. Li, T. Sun, C. Jiang, *Adv. Mater.* **2021**, *33*, 2100746; d) R. G. Canter, J. Penney, L.-H. Tsai, *Nature* **2016**, *539*, 187.

[9] a) Z. Du, M. Li, J. Ren, X. Qu, *Acc. Chem. Res.* **2021**, *54*, 2172; b) Z. Dhouafli, K. Cuanalo-Contreras, E. A. Hayouni, C. E. Mays, C. Soto, I. Moreno-Gonzalez, *Cell. Mol. Life Sci.* **2018**, *75*, 3521; c) Y. Liu, A. Aguzzi, *Science* **2019**, *364*, 130; d) M. G. Savelieff, G. Nam, J. Kang, H. J. Lee, M. Lee, M. H. Lim, *Chem. Rev.* **2019**, *119*, 1221; e) D. Kim, J. M. Yoo, H. Hwang, J. Lee, S. H. Lee, S. P. Yun, M. J. Park, M. Lee, S. Choi, S. H. Kwon, S. Lee, S.-H. Kwon, S. Kim, Y. J. Park, M. Kinoshita, Y.-H. Lee, S. Shin, S. R. Paik, S. J. Lee, S. Lee, B. H. Hong, H. S. Ko, *Nat. Nanotechnol.* **2018**, *13*, 812.

[10] a) C. H. van Dyck, *Biol. Psychiatry* **2018**, *83*, 311; b) E. E. Congdon, E. M. Sigurdsson, *Nat. Rev. Neurol.* **2018**, *14*, 399.

[11] a) I. F. do Valle, H. G. Roweth, M. W. Malloy, S. Moco, D. Barron, E. Battinelli, J. Loscalzo, A.-L. Barabási, *Nat. Food* **2021**, *2*, 143; b) H. Cao, L. Yang, R. Tian, H. Wu, Z. Gu, Y. Li, *Chem. Soc. Rev.* **2022**, *51*, 4175.

[12] a) F. L. Palhano, J. Lee, N. P. Grimster, J. W. Kelly, *J. Am. Chem. Soc.* **2013**, *135*, 7503; b) D. E. Ehrnhoefer, J. Bieschke, A. Boeddrich, M. Herbst, L. Masino, R. Lurz, S. Engemann, A. Pastore, E. E. Wanker, *Nat. Struct. Mol. Biol.* **2008**, *15*, 558; c) G. M. Pasinetti, U. H. Iqbal, P. B. Rosenberg, *Alzheimer's Dementia* **2020**, *16*, e044062; d) D. Sade Yazdi, D. Laor Bar-Yosef, H. Adsi, T. Kreiser, S. Sigal, S. Bera, D. Zaguri, S. Shaham-Niv, D. S. Oluwatoba, D. Levy, M. Gartner, T. D. Do, D. Frenkel, E. Gazit, *Proc. Natl. Acad. Sci. USA* **2021**, *118*, e2017575118; e) M. D. Navarro-Hortal, J. M. Romero-Márquez, A. Esteban-Muñoz, C. Sánchez-González, L. Rivas-García, J. Llopis, D. Cianciosi, F. Giampieri, S. Sumalla-Cano, M. Battino, J. L. Quiles, *Food Chem.* **2022**, *372*, 131272.

[13] a) F. F. de Araújo, D. de Paulo Farias, I. A. Neri-Numa, G. M. Pastore, *Food Chem.* **2021**, *338*, 127535; b) N. Meshginfar, H. Tavakoli, K. Dornan, F. Hosseinian, *Crit. Rev. Food Sci. Nutr.* **2021**, *61*, 1394.

[14] a) W. Zhang, A. Mehta, Z. Tong, L. Esser, N. H. Voelcker, *Adv. Sci.* **2021**, *8*, 2003937; b) G. C. Terstappen, A. H. Meyer, R. D. Bell, W. Zhang, *Nat. Rev. Drug Discovery* **2021**, *20*, 362; c) J. Zhou, T. R. Patel, R. W. Sirianni, G. Strohbehn, M.-Q. Zheng, N. Duong, T. Schafbauer, A. J. Huttner, Y. Huang, R. E. Carson, Y. Zhang, D. J. Sullivan, J. M. Piepmeier, W. M. Saltzman, *Proc. Natl. Acad. Sci. USA* **2013**, *110*, 11751.

[15] a) R. Yuan, Y. Li, S. Han, X. Chen, J. Chen, J. He, H. Gao, Y. Yang, S. Yang, Y. Yang, *ACS Cent. Sci.* **2022**, *8*, 10; b) R. Zhang, L. Cheng, Z. Dong, L. Hou, S. Zhang, Z. Meng, O. Betzer, Y. Wang, R. Popovtzer, Z. Liu, *Mater. Horiz.* **2021**, *8*, 1314; c) P. Yang, X. Zhou, J. Zhang, J. Zhong, F. Zhu, X. Liu, Z. Gu, Y. Li, *Green Chem.* **2021**, *23*, 1834.

[16] a) F. Behboodi-Sadabad, H. Zhang, V. Trouillet, A. Welle, N. Plumeré, P. A. Levkin, *Adv. Funct. Mater.* **2017**, *27*, 1700127; b) T. S. Sileika, D. G. Barrett, R. Zhang, K. H. A. Lau, P. B. Messersmith, *Angew. Chem., Int. Ed.* **2013**, *52*, 10766.

[17] P. B. Merkel, R. Nilsson, D. R. Kearns, *J. Am. Chem. Soc.* **1972**, *94*, 1030.

[18] H. Wang, X. Li, Y. Jiang, M. Li, Q. Xiao, T. Zhao, S. Yang, C. Qi, P. Qiu, J. Yang, Z. Jiang, W. Luo, *Angew. Chem., Int. Ed.* **2022**, *61*, e202200465.

[19] H. Huang, W. Gong, X. Wang, W. He, Y. Hou, J. Hu, *Adv. Healthcare Mater.* **2022**, *11*, 2102476.

[20] S. Kobayashi, H. Higashimura, *Prog. Polym. Sci.* **2003**, *28*, 1015.

[21] a) K. Debnath, A. K. Sarkar, N. R. Jana, N. R. Jana, *Acc. Mater. Res.* **2021**, *3*, 54; b) A. R. Araújo, J. Correa, V. Dominguez-Arca, R. L. Reis, E. Fernandez-Megia, R. A. Pires, *ACS Appl. Mater. Interfaces* **2021**, *13*, 59673.

[22] Z. Du, D. Yu, X. Du, P. Scott, J. Ren, X. Qu, *Chem. Sci.* **2019**, *10*, 10343.

[23] M. T. Heneka, R. M. Mcmanus, E. Latz, *Nat. Rev. Neurosci.* **2018**, *19*, 610.

[24] H. Wang, X. Xu, Y.-C. Pan, Y. Yan, X.-Y. Hu, R. Chen, B. J. Ravoo, D.-S. Guo, T. Zhang, *Adv. Mater.* **2021**, *33*, 2006483.

[25] H. Hampel, M.-M. Mesulam, A. C. Cuello, M. R. Farlow, E. Giacobini, G. T. Grossberg, A. S. Khachaturian, A. Vergallo, E. Cavedo, P. J. Snyder, Z. S. Khachaturian, *Brain* **2018**, *141*, 1917.

[26] Y. Leng, E. S. Musiek, K. Hu, F. P. Cappuccio, K. Yaffe, *Lancet Neurol.* **2019**, *18*, 307.

[27] M. Caffo, R. Fusco, R. Siracusa, G. Caruso, V. Barresi, R. Di Paola, S. Cuzzocrea, A. F. Germanò, S. M. Cardali, *Biomedicines* **2023**, *11*, 815.

[28] D. P. Behan, S. C. Heinrichs, J. C. Troncoso, X.-J. Liu, C. H. Kawas, N. Ling, E. B. De Souza, *Nature* **1995**, *378*, 284.

[29] Z. P. Wills, C. Mandel-Brehm, A. R. Mardinly, A. E. Mccord, R. J. Giger, M. E. Greenberg, *Neuron* **2012**, *73*, 466.

[30] K. Suzuki, J. Elegheert, I. Song, H. Sasakura, O. Senkov, K. Matsuda, W. Kakegawa, A. J. Clayton, V. T. Chang, M. Ferrer-Ferrer, E. Miura, R. Kaushik, M. Ikeno, Y. Morioka, Y. Takeuchi, T. Shimada, S. Otsuka, S. Stoyanov, M. Watanabe, K. Takeuchi, A. Dityatev, A. R. Aricescu, M. Yuzaki, *Science* **2020**, *369*, eabb4853.

[31] M. Tzioras, R. I. Mcgeachan, C. S. Durrant, T. L. Spires-Jones, *Nat. Rev. Neurol.* **2023**, *19*, 19.

[32] a) N. T. Fiore, S. R. Debs, J. P. Hayes, S. S. Duffy, G. Moalem-Taylor, *Nat. Rev. Neurol.* **2023**, *19*, 199; b) J. Karpf, P. Unichenko, N. Chalmers, F. Beyer, M.-T. Wittmann, J. Schneider, E. Fidan, A. Reis, J. Beckervordersandforth, S. Brandner, S. Liebner, S. Falk, A. Sagner, C. Henneberger, R. Beckervordersandforth, *Nat. Neurosci.* **2022**, *25*, 1626; c) S.-J. Lee, I. Depoortere, H. Hatt, *Nat. Rev. Drug Discovery* **2019**, *18*, 116; d) B. Dejanovic, T. Wu, M.-C. Tsai, D. Graykowski, V. D. Gandham, C. M. Rose, C. E. Bakalarski, H. Ngu, Y. Wang, S. Pandey, M. G. Rezzonico, B. A. Friedman, R. Edmonds, A. De Mazière, R. Rakosi-Schmidt, T. Singh, J. Klumperman, O. Foreman, M. C. Chang, L. Xie, M. Sheng, J. E. Hanson, *Nat. Aging* **2022**, *2*, 837.